The seasonal cycle of ERS scatterometer signatures over perennial Antarctic sea ice and associated surface ice properties and processes

Christian Haas
Alfred Wegener Institute for Polar and Marine Research
Columbusstrasse, D-27568 Bremerhaven, Germany
chaas@awi-bremerhaven.de

Abstract

Time series of satellite radar backscatter coefficients of the ERS-1/2 scatterometer are presented for perennial ice regions in the Antarctic from June 1991 to June 1999. There is a pronounced seasonal cycle, with higher backscatter in summer than in winter. On average, backscatter increases from spring values of –16.3 dB to summer values of –10.7 dB within 96 days. This rapid rise, and the summer maximum, are occasionally interrupted by sudden strong signal drops. After late summer/early fall, backscatter decreases again and slowly approaches winter values. The seasonal cycle is interpreted in terms of processes at the ice surface. The spring backscatter rise is associated with internal snow melt and the formation of superimposed ice. This process commences once the surface energy balance becomes positive. Sudden backscatter drops are caused by temporary melt water saturation of the snow during episodic events of warm air advection. In fall, when superimposed ice formation ceases due to surface cooling, gradual surface flooding with seawater becomes the dominating process. This causes the observed decreasing backscatter. The re-occurrence of the seasonal backscatter cycle in most regions points to the widespread formation of superimposed ice on perennial Antarctic sea ice.

Annals of Glaciology, Vol. 33, 69-73.

Introduction

Radar backscatter from sea ice is determined by volume- and surface-scattering of the ice and overlying snow. These depend on ice and snow properties such as salinity, porosity, grain size, wetness, and surface roughness. This allows the detection of multiyear ice in the Arctic, since it has higher backscatter coefficients than first-year ice due to its desalinated, porous surface ice (Onstott, 1992). Since the backscatter signature changes e.g. due to summer warming, the seasonal cycle of radar signatures can be utilised to monitor melt-onset and freeze-up in the Arctic (Barber and others, 1998; Winebrenner and others, 1998). The former is detectable by a sudden decrease in multiyear ice backscatter once air temperatures approach or exceed 0°C and the ice surface becomes saturated with melt water. Freeze-up is indicated by a slow return of backscatter coefficients to winter values.

In Antarctica, different ice types have also been identified based on their characteristic backscatter coefficients (Drinkwater and Haas, 1994; Drinkwater, 1998; Morris and others, 1998). Drinkwater and Liu (2000) used a drop of backscatter coefficients to map melt-onset over seasonal pack ice around Antarctica. In contrast to these observations, few studies have shown that backscatter from perennial ice in the Antarctic behaves opposite to the seasonal ice and to ice in the Arctic, since it is higher in summer than in winter (Drinkwater and Lytle, 1997; Drinkwater, 1998; Morris and others, 1998). A conclusive explanation for this is still missing.

Time series of European Remote Sensing (ERS) Satellite scatterometer data of perennial Antarctic sea ice are continuously available as weekly mean backscatter values around Antarctica. Consequently, the seasonal evolution of backscatter signatures can be described in detail. Based on ice core and snow data from perennial ice in summer (Haas and others, submitted) the seasonal cycle of backscatter signatures, and in particular the increased summer values, are subsequently addressed.

Satellite data analysis

ERS-1/2 scatterometer (ESCAT) data were obtained from the Polar Sea-Ice grids distributed on CD-ROM by the Centre ERS d'Archivage et de Traitment (CERSAT) of the Institut Francais pour l'Exploitation de la Mer (IFREMER), France. The data are weekly averages of VV-polarised, C-band (5.3 GHz / 5.7 cm) backscatter along 500 km wide swaths, which are projected onto a polar stereographic grid with a pixel size of approximately 25x25 km^2. Here, we used the backscatter coefficients normalised to an incidence angle of 40° (σ^0_{40}, after Gohin, 1995). Time series were computed for twelve perennial ice regions, from June 1991 to June 1999. Regions 1 to 7 are distributed from north to south in the western Weddell Sea, while Regions 8 to 12 cover the coastal area of the Bellingshausen, Amundsen, and Ross Seas (Fig. 1, Table 1).

At low ice concentrations (< 90%), pack-ice backscatter is biased by wind roughening of open water between ice floes (Drinkwater and Liu, 2000). To minimise this bias, only areas with high average February ice concentrations were taken into account

(Fig. 1). Ice concentration time series of the twelve regions were derived from DMSP SSM/I passive microwave data distributed by the National Snow and Ice Data Center (NSIDC) on CD-ROM (NSIDC, 1997). They are daily ice concentrations projected onto the same grid as the ESCAT data. Here, weekly mean concentrations were calculated corresponding to the weekly ESCAT data.

Because the analyses have been carried out on a fixed spatial grid, the derived variations may be partly due to seasonal changes and partly due to advection of ice with different surface properties. To overcome this uncertainty, backscatter values were additionally computed along selected ice drift trajectories, i.e. in a Lagrangian reference system, for a full year. Since no appropriate drift data were available from buoys, the drift trajectories were taken from numerical sea ice model calculations of Harder and Fischer (1999). The model was optimised for good agreement between observed and calculated ice drift.

Results

Figure 2 shows time series of backscatter and ice concentration for the twelve regions indicated in Figure 1, and the average of all regions. All regions show a strong seasonal cycle with increased summer backscatter. The sharp increase in November/December and the slow winter decrease is most obvious in the averaged time series. Spring rise and summer maximum are occasionally interrupted by sudden strong backscatter drops, usually lasting only for one week (Fig. 2). The distinct seasonal cycle is obviously independent of ice concentration, since it occurs even though ice concentrations remain close to 100% in many cases (Fig. 2). In other cases, the summer backscatter rise is not synchronous with ice concentration decreases.

Winter minima and summer maxima have been chosen from smoothed (3 point running average) time series as the local minima preceding and local maxima succeeding the spring rise, respectively, although this procedure is not always unequivocal. Table 1 summarises the main characteristics thus derived. On the average, backscatter increases from a winter minimum of –16.3 dB to a summer maximum of –10.7 dB during 96 days, commencing on day 319 (November 15). The differences between summer and winter backscatter are most pronounced in the northwestern Weddell Sea (regions 1-3) and in the Bellingshausen (region 8) and Ross Seas (regions 11, 12) (Fig. 2, Table 1).

The backscatter evolution along three selected drift trajectories for the years 1993 to 1995, commencing on October 1 at 74°S, 50°W, are portrayed in Figure 3. The drift was more or less northward and parallel to the Antarctic Peninsula. In all three cases, backscatter rises from about –17 dB in November to about –13 to –10 dB in February. There is a sudden weak backscatter drop at the end of January 1995. Backscatter decreases during fall and winter. However, in contrast to the cycles at fixed positions in Figure 2, backscatter of the Lagrangian measurements does not return to the spring values at the beginning of the drift. This is in agreement with the observed backscatter increase of the time series from regions 7 (South) to 1 (North) in Figure 2.

Discussion

From ice core and snow data of perennial sea ice in the Amundsen, Bellingshausen and Weddell Seas in February, Haas and others (submitted) propose a suite of processes taking place at the snow-ice interface during summer. They are governed by strong snow metamorphism and the extensive formation of superimposed ice due to internal snow melt and subsequent refreezing of downward percolating meltwater at the colder snow-ice interface. These processes commence once the energy budget at the snow surface becomes positive in spring. Superimposed ice contains air bubbles several millimetres in diameter, and its salinity is typically almost zero. The transition to the overlying coarse-grained and salt-free summer snow is very rough on the centimetre scale. These properties significantly enlarge the microwave volume and surface scattering intensities of the ice surface. Similar effects have been reported earlier by Holt and Digby (1985) and Onstott (1992). Therefore, we assume that the strong spring backscatter rise seen in Figures 2 and 3 coincides with the formation of superimposed ice.

A widespread phenomenon in the Antarctic is seawater flooding of the basal snow, when the ice surface is suppressed below the water level due to heavy snow loading (Eicken and others, 1994; Jeffries and others, 1997). However, Haas and others (submitted) found clear indication that superimposed ice formed also above the saline and cold flooded snow layer (often referred to as 'slush layer'), when the fresh melt water percolated onto the cold and saline slush. The process is similar to the formation of an ice layer at the meltwater/seawater interface of under-ice melt ponds in the Arctic (Eicken, 1994) by double diffusion. Thus, while seawater flooding alone would cause a decrease in backscatter, superimposed ice formation above the slush layer results in the opposite effect. This was not recognised by Drinkwater and Lytle (1997), although Lytle and Ackley (1996) showed that superimposed ice formed above the flooded snow during their study period in the northwestern Weddell Sea, too.

Snow melt on perennial Antarctic ice seems to be too weak to cause significant snow wetting, which would result in the attenuation of radar waves, as observed in the Arctic (Winebrenner and others, 1998; Barber and others, 1998). In fact, measurements of Haas and others (submitted) indicate that summer snow wetness is mostly less than 4%. However, the sudden backscatter drops in spring and summer indicate that, nevertheless, there are episodic phases of enhanced snow melt and melt water saturation. These result from the passage of large-scale synoptic systems causing advection of warm air masses (Morris and others, 1998). Soon afterwards, wetness decreases again, leaving behind larger snow grains and increased backscatter. The temporary backscatter drops in spring might also indicate seawater flooding events before superimposed ice formation commences (see above).

Superimposed ice formation leads to an upward-growing ice surface with resulting positive freeboard. This process competes with a steady submergence of floes due to bottom and internal melting, and surface accumulation of precipitation (Haas and others, submitted). Once superimposed ice formation ceases because of surface cooling

in early fall, submergence will become the dominating process. Thus, the freeboard of the ice surface will slowly become negative, and the well-known flood-freeze cycles during the cold season commence. This surface flooding with saline water will gradually attenuate radar waves at the incidence angle of EScat, and will cause the slow decline of backscatter during fall, winter and early spring. In those periods, the formation of new ice in between diverging perennial floes will also contribute to a decrease of backscatter coefficients.

As superimposed ice formation sets in once the surface energy balance reverses from negative to positive, it should be possible to monitor these reversals and their southward progression using scatterometer time series. It was shown above that, on average, backscatter begins to rise on day 319. However, in Table 1 no obvious temporal progression is visible from the northern towards the southern Weddell Sea. Only the magnitude of the seasonal cycle decreases towards the south, indicating less extensive snow melt and superimposed ice formation. The detection of an accurate rise date is hampered by averaging over one-week intervals, as well as by the inherent variability of the signal due to other effects. For example, roughening of the ice surface due to ice deformation causes higher backscatter as well (Drinkwater, 1998; Haas and others, 1999), and can therefore potentially hide any climatic effects on backscatter. In fact, the anomalous cycle in 1997, when backscatter remained high during much of the winter in the Weddell Sea (regions 2-7 in Figure 2), might have been caused by the observed high amount of ice ridging (Haas and others, 1999).

Conclusions

Radar backscatter from perennial Antarctic sea ice is shown to possess a strong seasonal cycle, with summer values exceeding winter backscatter by 5.6 dB on average over an eight-year period. The rapid backscatter rise in spring is suggested to be a result of the formation of superimposed ice which increases the volume and surface scattering contributions of the ice surface. The rise is only temporarily interrupted by short signal drops caused by melt water saturation of the snow during episodes of strong warm air advection. In fall, submergence of floes due to the mass of overlying snow leads to increasingly prevalent cycles of flooding and refreezing, thereby decreasing backscatter coefficients.

Superimposed ice formation commences once the snow is warmed beyond the freezing point. As the snow begins to melt, melt water refreezes above the ice surface. However, to cause a strong backscatter increase, melt has to be moderate without causing too much snow wetting. In contrast, melting of snow and ice in the Arctic and in the seasonal ice zone of the Antarctic is very fast, thus the backscatter drops sharply at the onset of summer melt. This scattering behaviour enables one to detect the melt onset and progression from time series of microwave signals (Barber and others, 1998; Winebrenner and others, 1998; Drinkwater and Liu, 2000). For perennial Antarctic sea ice the surface processes are more complex so that a relationship between the heat budget of the surface layer and backscatter coefficient is more difficult to derive.

The occurrence of the seasonal backscatter cycle in most test regions underlines the widespread occurrence of superimposed ice formation on perennial sea ice in Antarctica.

Acknowledgements

Satellite data provision by CERSAT/IFREMER and NSIDC is gratefully acknowledged. Markus Harder kindly provided drift vector fields from the sea ice model implemented at the Institut für Meereskunde, Kiel, Germany. I would like to thank Wolfgang Dierking for encouraging discussions, and Dave Thomas as well as Ernst Augstein for comments on the manuscript.

References

Barber, D.G., A. Thomas, and T.N. Papakyriakou. 1998. Role of SAR in surface energy flux measurements over sea ice. *In* Tsatsoulis, C., and R. Kwok, *eds. Analysis of SAR data of the polar oceans: Recent advances*. Springer-Verlag Berlin, Heidelberg, 35-68.

Drinkwater, M.R. 1998. Active microwave remote sensing observations of Weddell Sea ice. *In* Jeffries, M.O., *ed. Antarctic sea ice: physical processes, interactions and variability*. Antarctic Research Series, **74**, American Geophysical Union, 187-212.

Drinkwater, M.R., and C. Haas. 1994. Snow, sea-ice, and radar observations during ANT X/4: Summary data report. *Reports of the physics department*, **53**, Alfred Wegener Institute for Polar and Marine Research, Bremerhaven, Germany.

Drinkwater, M.R., and V.I. Lytle. 1997. ERS-1 SAR and field-observed characteristics of austral fall freeze-up in the Weddell Sea, Antarctica. *J. Geophys. Res.,* **102**(C6), 12593-12608.

Drinkwater, M.R., and X. Liu. 2000. Seasonal to interannual variability in Antarctic sea-ice surface melt. IEEE Trans. Geosci. and Remote Sensing, **38**(4), 1827-1842.

Eicken, H., M.A. Lange, H.W. Hubberten, and P.Wadhams. 1994. Characteristics and distribution patterns of snow and meteoric ice in the Weddell Sea and their contribution to the mass balance of sea ice. *Ann. Geophys.*, **12**(1), 80-93.

Eicken, H. 1994. Structure of under-ice melt ponds in the central Arctic and their effect on the sea ice cover. *Limnol. Oceanogr.*, **39**, 682-694.

Gohin, F. 1995. Some active and passive microwave signatures of Antarctic sea ice from mid-winter to spring 1991. *Int. J. Rem. Sens.*, **16**(11), 2031-2054.

Haas, C., Q. Liu, and T. Martin. 1999. Retrieval of Antarctic sea-ice pressure ridge frequencies from ERS SAR imagery by means of in-situ laser profiling and usage of a neural network. *Int. J. Remote Sensing*, **20**(15--16), 3111-3123.

Haas, C., D.N. Thomas, and J. Bareiss. 2000. Surface properties and processes of perennial Antarctic sea ice in summer. *J. Glaciol.*, to be submitted.

Harder, M., and H. Fischer. 1999. Sea ice dynamics in the Weddell Sea simulated with an optimized model. *J. Geophys. Res.*, 104(C5), 11151-11162.

Holt, B., and S.A. Digby. 1985. Processes and imagery of first-year fast sea ice during the melt season. *J. Geophys. Res.*, **90**(C3), 5045-5062.

Jeffries, M.O., A.P. Worby, K. Morris, and W.F. Weeks. 1997. Seasonal variations in the properties and structural composition of sea ice and snow cover in the Bellingshausen and Amundsen Seas, Antarctica. *J. Glaciol.*, **43**(143), 138-151.

Lytle, V.I., and S.F. Ackley. 1996. Heat flux through sea ice in the western Weddell Sea: Convective and conductive transfer processes. *J. Geophys. Res.*, **101**(C4), 8853-8868.

NSIDC (National Snow and Ice Data Center). 1997. Passive microwave derived daily polar sea ice concentration time series. Digital data available from nsidc@kryos.colorado.edu. Boulder, Colorado. NSIDC Distributed Active Archive Center, University of Colorado at Boulder.

Onstott, R.G. 1992. SAR and scatterometer signatures of sea ice, in *Microwave remote sensing of sea ice*, edited by F.D. Carsey, pp. 73-104, AGU Monograph **68**, 1992.

Winebrenner, D.P., D.G. Long, and B. Holt. 1998. Mapping the progression of melt onset and freeze-up on Arctic sea ice using SAR and Scatterometry. *In* Tsatsoulis, C., and R. Kwok, *eds. Analysis of SAR data of the polar oceans: Recent advances*. Springer-Verlag Berlin, etc., 129-144.

Figure captions

Figure 1: Map of the West Antarctic, showing the location of 12 test regions where backscatter time series were computed (Fig. 2). Grey shading indicates the mean February ice concentration (C) from 1992 to 1999, derived from satellite passive microwave data (SSM/I).

Figure 2: Time series of weekly mean backscatter coefficients at 40° incidence angle and ice concentration in the perennial ice regions shown in Figure 1, and for all regions averaged (bottom right). Arrows point to some sudden backscatter drops typical for summer signatures.

Figure 3: Backscatter evolution and ice concentration along three drift trajectory derived from model results of Harder and Fischer (1999), starting at 74°S, 50°W on October 1, 1993, 1994, and 1995, respectively.

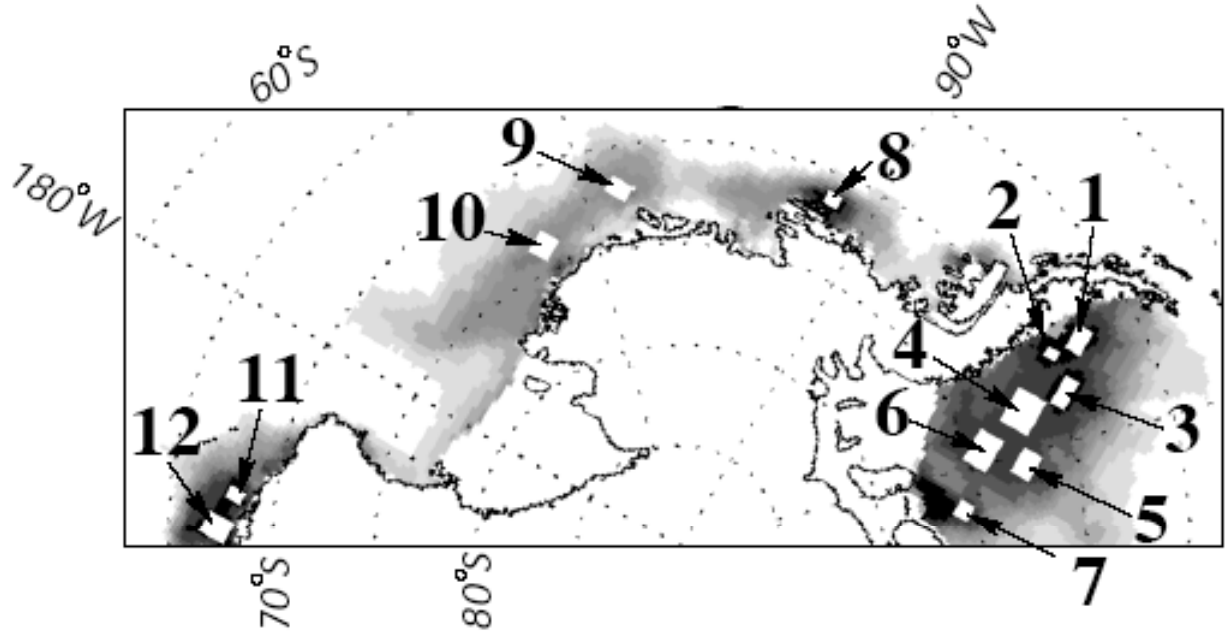

Figure 1: Map of the West Antarctic, showing the location of 12 test regions where backscatter time series were computed (Fig. 2). Grey shading indicates the mean February ice concentration (C) from 1992 to 1999, derived from satellite passive microwave data (SSM/I).

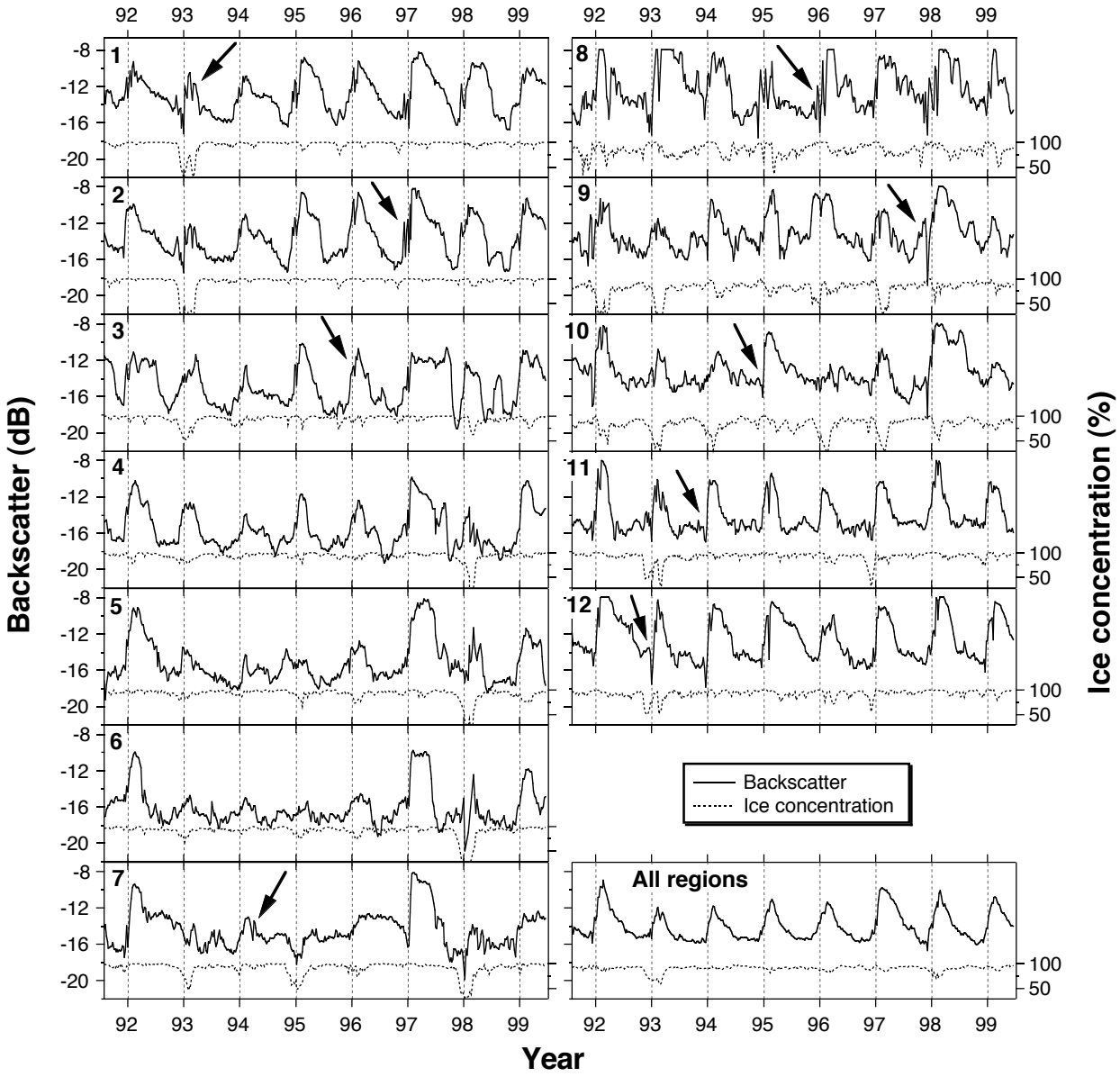

Figure 2: Time series of weekly mean backscatter coefficients at 40° incidence angle and ice concentration in the perennial ice regions shown in Figure 1, and for all regions averaged (bottom right). Arrows point to some sudden backscatter drops typical for summer signatures.

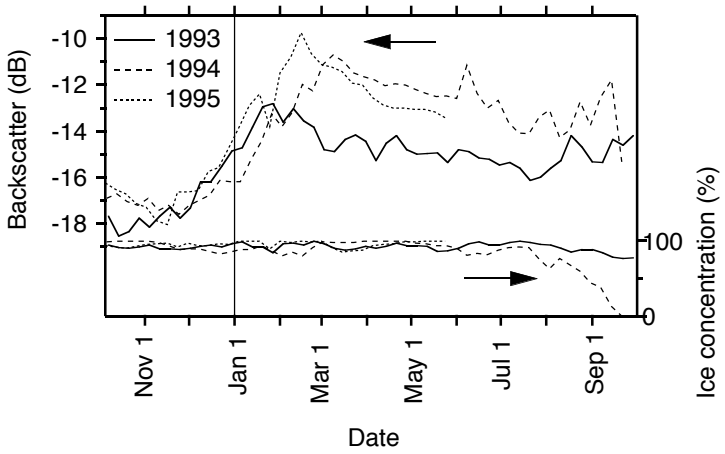

Figure 3: Backscatter evolution and ice concentration along three drift trajectory derived from model results of Harder and Fischer (1999), starting at 74°S, 50°W on October 1, 1993, 1994, and 1995, respectively.

Table 1: Main characteristics of the seasonal backscatter cycle in the twelve regions of Figures 1 and 2 (mean ± 1 standard deviation). Rise time is the period between melt onset and the first local summer maximum (see text).

Region	Latitude (°S)	Longitude (°W)	Size (Pixel)	Winter backscatter (dB)	Summer backscatter (dB)	Difference summer-winter (dB)	Melt-onset (Day)	Rise time (Days)
1	67.59	57.04	15	-15.9±0.8	-9.8±0.9	6.1±1.1	308±29	111±35
2	69.01	57.43	9	-16.3±0.9	-9.9±1.4	6.3±1.9	310±13	102±16
3	69.37	51.29	18	-17.8±0.8	-11.6±0.8	6.2±0.7	303±24	106±38
4	71.61	51.06	48	-17.7±0.8	-12.2±1.6	5.5±1.8	293±34	115±33
5	72.18	43.44	20	-17.0±0.6	-12.2±2.2	4.8±1.9	308±63	99±59
6	73.93	47.31	35	-17.4±0.9	-13.3±2.3	4.1±2.1	299±42	118±34
7	75.42	37.32	9	-16.7±1.0	-12.5±2.3	4.2±2.2	358±25	65±27
8	71.27	95.26	6	-15.0±0.8	-8.5±0.8	6.5±1.2	328±33	90±34
9	72.07	128.26	12	-15.3±0.8	-9.9±1.4	5.4±1.4	315±39	104±48
10	73.79	143.05	20	-15.2±0.5	-10.6±1.8	4.7±2.2	339±25	83±23
11	68.49	156.56	6	-15.8±0.4	-9.9±1.1	5.9±1.1	335±15	70±17
12	67.72	152.26	20	-15.1±0.5	-8.7±0.8	6.4±0.9	334±19	89±21
All				-16.3±1.2	-10.7±2.1	5.6±1.7	319±36	96±36